

1 Antarctic Bottom Water warming and freshening: Contributions to sea level rise,
2 ocean freshwater budgets, and global heat gain*

3 SARAH G. PURKEY^{1,2,3} and GREGORY C. JOHNSON^{2,1}

4

5 ¹*School of Oceanography, University of Washington, Seattle WA 98195, USA*

6 ²*NOAA/Pacific Marine Environmental Laboratory, Seattle WA 98115, USA*

7

8 *for Journal of Climate*

9 submitted 26 November 2012

10 revised 8 February 2013

10

* Pacific Marine Environmental Laboratory Contribution Number 3954

³*Corresponding author address:* Sarah G. Purkey, School of Oceanography, Box
357940, University of Washington, Seattle WA 98195-7940, USA. E-mail:
sarah.purkey@noaa.gov.

Abstract:

Freshening and warming of Antarctic Bottom Water (AABW) between the 1980s and 2000s are quantified, assessing the relative contributions of water-mass changes and isotherm heave. The analysis uses highly accurate, full-depth, ship-based, conductivity-temperature-depth measurements taken along repeated oceanographic sections around the Southern Ocean. Fresher varieties of AABW are present within the South Pacific and South Indian oceans in 2000s compared to the 1990s, with the strongest freshening in the newest waters adjacent to the Antarctic continental slope and rise indicating a recent shift in the salinity of AABW produced in this region. Bottom waters in the Weddell Sea exhibit significantly less water-mass freshening than those in the other two southern basins. However, a decrease in the volume of the coldest, deepest waters is observed throughout the entire Southern Ocean. This isotherm heave causes a salinification and warming on isobaths from the bottom up to the shallow potential temperature maximum. The water-mass freshening of AABW in the Indian and Pacific sectors is equivalent to a freshwater flux of $73 \pm 26 \text{ Gt yr}^{-1}$, roughly half of the estimated recent mass loss of the West Antarctic Ice Sheet. Isotherm heave integrated below 2000 m and south of 30°S equates to a net heat uptake of $34 \pm 3 \text{ TW}$ of excess energy entering the deep ocean from deep volume loss of AABW and $0.37 \pm 0.15 \text{ mm yr}^{-1}$ of sea level rise from associated thermal expansion.

1. Introduction

Antarctic Bottom Water (AABW) is the Southern Ocean's coldest, densest water mass. It ventilates the lower limb of the Meridional Overturning Circulation (MOC; e.g. Lumpkin and Speer 2007), filling most of the world's deep basins (Johnson 2008). In recent decades AABW has warmed (e.g. Purkey and Johnson 2010; hereafter P&J 2010), freshened (e.g. Johnson et al. 2008; Swift and Orsi 2012), and decreased in volume (e.g. Kouketsu et al. 2011; Purkey and Johnson 2012, hereafter P&J 2012), possibly linked to the increase in the glacial melt fresh water fluxes into AABW formation regions around Antarctica (e.g. Jacobs and Guilivi 2010). The freshening decreases the salinity of the shelf waters, thence AABW, and appears to slow AABW production and thus the lower limb of the MOC. Here we examine AABW property changes throughout the Southern Ocean, separating the component owing to θ - S (potential temperature-salinity) changes from that due to changes in the depth of potential isotherms (heave). Heave reflects changes in AABW volume, related to changes in the formation rate, circulation, or perhaps even formation properties of AABW. A shift in the θ - S curve indicates a change in water-mass properties. Decomposing the observed deep changes into these components allows for evaluation of the relative contributions of these changes to local Sea Level Rise (SLR), freshwater, and heat budgets.

AABW is a combination of very cold and relatively fresh water formed on shallow continental shelves and warmer, saltier offshore Circumpolar Deep Water (CDW; Foster and Carmack 1976). The shelf waters form over shallow ice-covered continental shelves where brine rejection from sea ice formation and export

increases the salinity of surface waters. This water sinks, mixing with adjacent CDW, and circulates under the ice shelf, melting the overlying ice at depth, causing the shelf waters to freshen (Jacobs 2004). These processes result in a reservoir of very cold, dense shelf water that, when it leaves the shelf, flows down the continental slope, further mixing with CDW (Jacobs 2004).

AABW formation occurs in the Ross Sea, Adelie Coast, and Weddell Sea, producing three distinct varieties of AABW (Orsi et al. 1999): Ross Sea Bottom Water (RSBW), Adelie Land Bottom Water (ALBW), and Weddell Sea Bottom Water (WSBW). These water masses mix with overlying CDW in the Antarctic Circumpolar Current (ACC) before feeding into the lower limb of the MOC and traveling to the northern ends of the Pacific, West Atlantic, and Indian oceans (Johnson 2008).

AABW is often defined as water with neutral density $\gamma_n > 28.27 \text{ kg m}^3$ found south of the SubAntarctic Front (SAF; Orsi et al. 1999). Here we use an older definition for AABW of deep Southern Ocean waters of $\theta < 0^\circ\text{C}$ (e.g. Gordon 1972), because we use θ , rather than γ_n , as a vertical coordinate.

AABW freshening has been observed (Aoki et al. 2005; Jacobs and Giulivi 2010; Swift and Orsi 2012) and slowdown of AABW formation rates inferred (P&J 2012) in the Ross Sea and Australian-Antarctic Basin starting as early as the 1950s. Ross Sea Shelf Water, an important constituent of RSBW, has freshened by 0.03 decade^{-1} between 1958 and 2008 (here salinity is reported on the 1978 Practical Salinity Scale (PSS-78) a dimensionless scale derived from the conductivity of the sampled seawater). This freshening is associated with freshening of the coastal current connecting the Amundsen Coast to the Ross Sea Shelf (Jacobs and Giulivi 2010).

Along the west side of the Ross Gyre, within the deep western boundary current transporting the recently formed RSBW northwestward, the densest water seen in 1994 completely disappeared by 2011, the deep and surface constituents of the shelf water freshened, and thickness of the RSBW outflow decreased by a few hundred meters (Swift and Orsi 2012). Directly downstream from its formation region in the Australian-Antarctic Basin, ALBW has freshened by 0.03 PSS-78 between 1994 and 2002 (Aoki et al. 2005). In the deep Australian-Antarctic Basin, ventilated by both RSBW and ALBW, freshening is evident throughout the basin, owing either to fresher bottom water or different ratios of RSBW and ALBW (Whitworth III 2002; Rintoul 2007; Johnson et al. 2008). In both the Australian-Antarctic Basin and the Ross Sea, cooling on isopycnals and warming on isobars are also present (Aoki et al. 2005; Johnson et al. 2008; Jacobs and Guilivi 2010; P&J 2010).

In the Weddell Sea, bottom water and deep water have been warming with little change in salinity (Robertson et al. 2002; Fahrbach et al. 2004; 2011; P&J 2010). To the north, the deep waters in the Scotia Sea and Argentine Basin, both directly fed by WSBW, have warmed and decreased in volume for at least the past three decades (Coles et al. 1996; Johnson and Doney 2006; Meredith et al. 2008; P&J 2012).

Outside the Southern Ocean, the abyssal waters along the bottom limb of the MOC fed by AABW (Johnson 2008), have warmed around the globe (P&J 2010; Kouketsu et al. 2011). The global-scale warming could be caused by a decrease in AABW formation rates, causing isopycnals to fall, hence the observed warming on isobaths. This signal can be communicated remotely by planetary waves

throughout the world ocean on much shorter time scales than advective changes (Masuda et al. 2010; Kouketsu et al 2011; P&J 2012). AABW warming has been analyzed in the Western South Atlantic (Johnson and Doney 2006; Zenk and Morozov 2007), throughout the Pacific (Fukasawa et al. 2004; Johnson et al. 2007; Kawano et al. 2010) and in the eastern Indian Ocean (Johnson et al. 2008; P&J 2010).

Much of the recent AABW property changes observed around the globe may be owing to increased glacial freshwater discharge from a number of locations around Antarctica over recent decades (e.g. Jacobs and Guilivi 2010). Antarctic ice shelf thinning and glacial discharge acceleration are strongest along the West Antarctic Peninsula and the Amundsen Coast (Rignot and Jacobs 2002; Rignot et al. 2008), with a net ice sheet loss of $88 \pm 54 \text{ Gt yr}^{-1}$ in the West Antarctic and $60 \pm 46 \text{ Gt yr}^{-1}$ along the peninsula between 1992–2006 (Rignot et al. 2008). Between 1991 and 2001 $154 \pm 16 \text{ km}^3$ of glacier ice was lost to the Amundsen Sea with acceleration of coastward glacier flow (Shepherd et al. 2002). At Pine Island Glacier, a location with one of the highest melt rates, the ice shelf has recently been thinning at a rate of 5.5 m yr^{-1} through basal melting owing to a $0.5 \text{ }^{\circ}\text{C}$ warming of ocean waters under the ice shelf (Shepherd et al. 2004). Similarly, along the Amundsen and Bellingshausen coasts where warm CDW has access to the shelf, the melting rates on the submerged undersides of glaciers have been correlated with warming ocean temperatures, with melting increasing by 1 m per $0.1 \text{ }^{\circ}\text{C}$ of warming (Rignot and Jacobs 2002).

The observed AABW property and circulation changes are important for global heat and SLR budgets (P&J 2010; Kouketsu et al 2011). The deep ocean warming

below 4000 m globally is equivalent to a net heat uptake of $0.027 \pm 0.009 \text{ W m}^{-2}$ over the surface the Earth and 0.05 mm yr^{-1} mean global SLR (P&J 2010). In the Southern Ocean, the warming below 1000 m is equivalent to as much as a 1.2 W m^{-2} local heat flux and 1.3 mm yr^{-1} local SLR (P&J 2010).

Here we evaluate salinity and temperature changes within the deep Southern Ocean, distinguishing between heave and water property changes. Section 2 discusses the data set and processing, including inter-cruise salinity adjustments (see also Appendix A). Section 3 presents methods used to distinguish heave from water-mass changes. Section 4 discusses freshening trends throughout the Southern Ocean, using multiple Southern Ocean sections occupied two or more times since the 1980s. Section 5 estimates basin-mean rates of change to find the contributions of the deep Southern Ocean to changes in SLR, heat budgets and freshwater budgets. Section 6 discusses these results.

2. Data and Processing

We use full-depth, high-resolution, highly accurate, ship-based hydrographic data collected in the Southern Ocean since 1980 at locations with two or more occupations. The data were mostly collected as part of the international World Ocean Circulation Experiment (WOCE) Hydrographic Programme or the Global Ocean Ship-based Hydrographic Investigation Program (GO-SHIP). All publicly available data at <http://cchdo.ucsd.edu> as of November 2012 are considered here. We refer to each section by its WOCE ID (Fig. 1, Table A1). All data collected along a section within a year are combined and referred to as a single occupation of that

section, referenced by the calendar year in which the earliest station was taken (Table A1).

We focus on sections located at or south of 30 °S (Fig. 1): nine meridional sections roughly spaced every 45° longitude, two zonal sections at ~67 °S across the Ross Sea and the Weddell Sea, and three zonal sections that together completely circumnavigate the globe near 30 °S (Fig. 1). Most of the meridional sections in the Indian and Atlantic sectors extend to the Antarctic continental shelf, but both of the sections in the Pacific sector stop short of the shelf (Fig. 1). Along each section data were collected from the surface to approximately 10 m from the bottom at stations nominally spaced every 55 km. Each re-occupation of a given section analyzed here lies within 10 km of the original. Data along each section are interpolated onto an evenly spaced 20-dbar vertical and 2' horizontal grid following P&J (2010).

Data were collected between 1980 and 2012, with the length-weighted mean first occupation in 1991 and the last in 2008. Each section has been occupied between two and eight times with the length-weighted mean and median for the study region of 3.6 and 3.0 occupations, respectively (Table A1). Therefore, the along-section trends discussed here span on average an 18-year period. Most trend estimates are based on data from at least three occupations; however, some trends are based on the difference between two occupations (Table A1).

All data were collected with a Conductivity-Temperature-Depth (CTD) instrument with target measurement accuracy better than 0.002 °C for temperature, 3 dbar for pressure, and 0.002 PSS-78 for salinity (Joyce 1991). All CTD temperature data were reported in, or converted to, the 1968 International Practical

Temperature Scale (IPTS-68) for use with the 1980 Equation of State (EOS-80). The CTD salinity measurements were all standardized with International Association for Physical Science of the Oceans (IAPSO) Standard Seawater (SSW), with all salinity values reported here on PSS-78. We consider only data with good quality flags and remove any obvious spikes in salinity data.

We apply known salinity offsets owing to the different IAPSO SSW batches used on the different cruise legs to the salinity data (Table A1). Batch-to-batch offsets are from Kawano et al. (2006) and T. Kawano (personal communication 2011). They range from -1.2×10^{-3} to 2.5×10^{-3} PSS-78 (Table A1). SSW offsets could not be applied to 13 of the 73 Southern Ocean cruise legs analyzed here owing to 8 legs having no SSW batch number information available and 5 cruises using SSW batches too recent to have an offset estimate.

Additional ad-hoc salinity adjustments are estimated and applied to the CTD salinity data to further minimize intercruise measurement biases (Appendix A, Table A1, Figure A1). These salinity offsets are calculated by comparing salinity data in select geographical regions containing water that has been isolated from the surface for a relatively long time and is hence well-mixed with a very tight (low variance) θ -S relation (Appendix A). These additional offsets are necessary because of the relatively large contribution of salinity to density and the relatively high ratio of measurement error to signal observed here (Appendix A).

The ad-hoc salinity offsets are applied to 67 of the 73 Southern Ocean legs with magnitudes ranging from essentially zero ($< 10^{-6}$ PSS-78) to as high as 0.0056 PSS-78, with 63 of the applied offsets being less than the WOCE target accuracy of

0.002 PSS-78 (Fig. A1). The four legs with offset magnitudes > 0.002 PSS-78 are the 1984 occupation of P16, the 1993 and 1995 occupations of S03, and the 2011 occupation of A16 (Fig. A1; Table A1). A salinity offset could not be applied to six legs. These legs include the three occupations of S01 through the Drake Passage (Fig. 1) where highly variable water properties did not allow a suitable place for intercruise comparisons. Also three subsections of full lines are not long enough for salinity comparisons, namely the 1995, 2006, and 1991 occupations of I09, P18, and S03, respectively. The salinity offsets are applied to the raw CTD salinity data and each section occupation is re-gridded vertically and horizontally (P&J 2010).

3. Methods: Heave vs. Water Property Changes

Interior ocean property changes can be caused by heave or water-mass changes (e.g., Fig. 2). A number of methods have been deployed for distinguishing between heave and water-mass changes. For example, Bindoff and McDougall (1994) decompose ocean property changes using S and θ changes on both density and pressure surfaces and the original θ - S curve to solve for the contributions of isopycnal heave, freshening, and salinification, whereas McDonagh et al. (2005) calculate water-mass changes by calculating the "minimum distance" between chronological θ - S curves, scaling them by thermal expansion and haline contraction coefficients.

Here we use θ as the independent variable instead of density to allow detection of very small deep θ - S changes. We make this choice because S errors have significantly more impact on density than θ errors, especially in cold deep

waters. For example, at 4000 m in the Ross Sea, the expected measurement salinity error of 0.002 PSS-78 will cause an error in density fifteen times larger than the expected temperature error of 0.001 °C would cause. Therefore we choose the most accurate measurement, θ , to be the independent variable in our analysis, rather than density, which would amplify any remaining S errors.

As a result of this choice, here heave refers to a vertical shift of the water column caused by a change in depth (equivalently pressure) of a potential isotherm that has no effect on the local θ -S relationship (Fig. 2b). Alternatively, a water-mass change is reflected in a shift in the shape of the θ -S curve with time (e.g. Fig. 2a). If density surfaces were used as the vertical coordinate, water mass and heave changes reported here would be amplified, as salinity generally decreases with decreasing temperature within AABW in the Southern Ocean.

While this method clearly identifies where θ -S changes occur, it casts all the water-mass changes in terms of salinification (or freshening) and all warming (or cooling) as owing to heave. For example, imagine a scenario in the deep Southern Ocean (where θ decreases and S increases with increasing depth) where the whole water column warms, causing the θ -S curve to be displaced upwards. Our analysis would cast this water-mass change as freshening, with a value proportional to the warming by the local slope of the θ -S curve. While deep AABW freshening presented here is traced back to the shelf water changes that are freshening faster than warming (e.g., Jacobs and Guilivi 2010), the limitations of our method should be kept in mind.

To decompose the deep property changes, first we define an initial θ -S

238 relation (θ - S_i) representative of the θ - S at the time of the first occupation at every
239 location along a section. Each vertical profile of S and θ of each section is linearly
240 interpolated onto an evenly spaced θ grid from -2 to 5 °C at 0.01 °C intervals. The
241 interpolation extends from the bottom to the first θ maximum (usually the θ -
242 maximum associated with CDW). All values above the maximum are masked out.
243 The bottom S value of each interpolated S profile is extended to the minimum
244 bottom θ measured at that location among all occupations of the section by using
245 the slope of the linear fit of S vs. θ over the coldest 0.1 °C of each profile. This
246 extension is only applied if the bottom $\theta < 3$ °C, the profile depth > 500 m, and the
247 bottom 0.1 °C spans more than 100 m of the water column. These criteria limit
248 extensions to deeper offshore regions, excluding thermocline or continental shelf
249 waters. Finally, S_i at each θ -grid is estimated for the time of the first occupation
250 from linear fits of S vs. time for all occupations. If there are only two occupations,
251 then S_i matches S of the first occupation, but if there are multiple occupations of a
252 section, then S_i will differ from S of the first occupation.

253 The θ - S_i relations are used to calculate expected S values, S_H , if heave were
254 the only contributor to the changes in S . At each vertical and horizontal gridpoint
255 for each occupation, a value of S_H is computed from θ using a spline interpolant and
256 the local θ - S_i relation.

257 Finally, we calculate S rates of change for the total (S_T), S_H , and water-mass
258 shift (S_{WM}) with time and associated error as follows. At every horizontal and
259 vertical grid point along each section with at least two occupations spanning more
260 than 2.5 years (following P&J 2010) the rate of change of total S with time (dS_T/dt)

and dS_H/dt are estimated by linear least-squares (e.g. Fig. 3). Where only two occupations exist, the rates of change reflect differences between these two occupations. Within the Southern Ocean below 300 m, the trend error along sections with more than two occupations is usually less than 0.4×10^{-3} PSS-78 yr^{-1} , smaller than most of the along-section signal (e.g. Fig. 3). The rate of change in salinity with time owing to water-mass shifts, $dS_{WM}/dt = dS_T/dt - dS_H/dt$, is calculated along each section (e.g. Fig. 3a,d,g,j,m). In addition, the rate of change of θ with time ($d\theta/dt$) is found also using a linear least-squares fit (not shown, see P&J 2010).

For each deep basin (following P&J 2012; Fig. 1), the rates along all sections within a given basin are used to find basin-mean rates and associated errors within 0.05 °C-thick bins below 5 °C. Along each section within a basin, using the mean θ from all occupations, a θ -bin is identified as the region where θ falls within ± 0.025 of a given value. Within each θ -bin area, first the vertical mean $d\theta/dt$, dS_T/dt , dS_{WM}/dt , and dS_H/dt are calculated along the sections. The vertical length of the given θ -bin at each location along the section is used to find a horizontal length-weighted mean rate (hereafter basin mean rates) for each θ -bin using all sections within a basin as if they were lined up end-to-end. The horizontal variance along a θ -bin is much larger than the vertical variance within a θ -bin. Therefore, we calculate and use the horizontal standard deviation of the vertical mean rates along a given isotherm (hereafter, basin standard deviations) for the basin error analyses. The basin standard deviations are also calculated as if all sections within a basin were connected end-to-end, a more conservative choice than the section length-

weighted mean technique used in P&J (2010). In addition, the basin standard deviations are usually larger than the slope errors on the rates themselves. Slope errors are neglected in the final error analysis, since they cannot be determined for most sections. Finally the degrees of freedom (DOF) for each isotherm bin are calculated using the horizontal length of the θ -bin following P&J 2010 assuming a 163-km decorrelation length scale (P&J 2010). The 95% confidence intervals are found for each basin for each θ -bin assuming a Student's t-distribution (e.g. Fig. 4).

The 95% confidence intervals reported here are based on the spatial variance of trends along the sections and do not fully resolve the error associated with temporal variability in the trend. However, as noted earlier, the trend errors in time along sections with more than two occupations (the majority of the sections analyzed) are generally smaller than the signal. In addition, the consistent patterns seen throughout the Southern Ocean in all sections analyzed (section 4), all occupied over varying time periods, increases confidence that the basin mean rates reported here reflect a fairly consistent decadal change, at least from the 1980s through the 2000s. Furthermore, in the few areas with better temporal sampling, fairly steady AABW warming has been observed over the past few decades (e.g., Zenk and Morozov 2007). However, to resolve fully the temporal variability and determine if the changes are associated with a secular trend, an oscillation, or have a more complex temporal pattern over the 30-year reporting period would require a higher temporal resolution large-scale data set.

4. Results

307 Throughout the Southern Ocean, water colder than 0 °C in each of the deep
308 basins is freshening owing to water-mass changes, albeit in varying amounts, and
309 becoming saltier below the CDW S-maximum owing to heave. The net effect is a
310 deep freshening in the Indian and Pacific below 0°C with salinification above (Fig.
311 3a–l; Fig. 4b–c). In the South Atlantic, heave dominates to effect a nearly full water
312 column salinification (Fig. 3m–o; Fig. 4a).

313 In the South Pacific, water-mass freshening dominates the total S signal in
314 waters of $\theta < 0$ °C throughout the Ross Gyre (west of 140°W; Fig 3a,b,c), with
315 freshening increasing by an order of magnitude to $3 (\pm 2) \times 10^{-3}$ PSS-78 yr⁻¹ in the
316 waters along the continental rise on the western side of the basin where the purest
317 and most recently formed RSBW flows westward (Jacobs and Gili 2010). This
318 strongest freshening along the continental rise in the coldest waters ($\theta < -0.4$ °C) is
319 almost completely owing to water-mass shifts (Fig. 4f), and is consistent with the
320 total freshening reported by Swift and Orsi (2012) in this region. Within the interior
321 of the Ross Gyre, water-mass freshening is $\sim 0.2 \times 10^{-3}$ PSS-78 yr⁻¹ for $\theta < 0$ °C (Fig.
322 3a; Fig. 4c). The heave component causes an $\sim 0.03 \times 10^{-3}$ PSS-78 yr⁻¹ salinification
323 between the bottom and 1000 m (Fig. 3b; Fig. 4c) owing to a reduction in the
324 volume of the coldest bottom waters, significantly different from zero at 95%
325 confidence in the basin mean for $0.2 < \theta < 0.9$ °C. These two counteracting factors
326 combine such that water-mass freshening dominates for $\theta < 0$ °C, with a net
327 freshening of 0.16×10^{-3} PSS-78 decade⁻¹, while heave dominates between 0°C and
328 1000 m causing a net salinification (Fig. 3c; Fig. 4c,f). The Amundsen Basin (east of
329 140°W) exhibits a slight water-mass freshening and heave salinification for zero net

change in salinity along S4P (Figs. 3a–c) and in the two meridional sections that cross the basin (Fig. 1; not shown).

In the South Indian, water-mass freshening is present throughout AABW (Fig 3d,g,j), strongest along the continental slope, where recently formed RSBW and ADLW flow westward before flowing north, ventilating the deep Australian-Antarctic Basin (Orsi et al. 1999). Consistent with previous studies (Aoki et al. 2005; Rintoul 2007; Johnson et al. 2008; Jacobs and Gili 2010; Shimada et al. 2012), our results show a strong water-mass freshening, with basin-mean rates ranging from $1.2 (\pm 0.6) \times 10^{-3}$ PSS-78 yr^{-1} within the coldest ($\theta \sim -0.5$ °C) bottom water to $0.2 (\pm 0.1) \times 10^{-3}$ PSS-78 yr^{-1} at $\theta = 0$ °C (Fig. 4b,e). The freshening signal in the bottom waters ($\theta < -0.2$ °C) becomes gradually fainter from west to east: starting at $\sim 0.6 \times 10^{-3}$ PSS-78 yr^{-1} in S03 (Fig. 3d, $\sim 140^\circ\text{E}$), to $\sim 0.5 \times 10^{-3}$ PSS-78 yr^{-1} in I09 (Fig. 3g, $\sim 115^\circ\text{E}$), to $\sim 0.3 \times 10^{-3}$ PSS-78 yr^{-1} in I08 (Fig. 3j, $\sim 90^\circ\text{E}$). Again, heave partially counteracts this freshening in all sections (Fig. 3e,h,k). The basin mean dS_H/dt accounts for $\sim 0.15 \times 10^{-3}$ PSS-78 yr^{-1} of salinification, statistically significantly different from zero for $-0.3 < \theta < 0.5$ °C (Fig. 4b,e). The basin-mean dS/dt shows a net freshening for $\theta < 0$ °C and mostly a net salinification for $\theta > 0$ °C (Fig. 3f,i,l; Fig. 4b,e).

In the South Atlantic, less water-mass freshening is observed with more heave salinification, causing a very slight, and statistically insignificant net salinification of $\sim 0.1 (\pm 0.13) \times 10^{-3}$ PSS-78 yr^{-1} throughout the deep waters ($\theta < 0.4$ °C; e.g. Fig. 3 m,n,o; Fig. 4a,d). The zonal SR04 section across the Weddell Gyre exhibits the most consistent trend among the sections crossing the Weddell-

353 Enderby Basin with a water-mass freshening of $\sim 0.05 \times 10^{-3}$ PSS-78 yr^{-1} in the
354 interior and slightly higher values along its east and west flanks, where the deep
355 westward flow of the southern limb of the Weddell Gyre and the northward-flowing
356 current carrying recently formed WSBW are found, respectively (Gordon et al.
357 2010). The heave, however, causes a bottom intensified salinification of $\sim 0.1\text{--}0.3 \times$
358 10^{-3} PSS-78 yr^{-1} throughout much of the water column, consistent with a decrease in
359 the volume of WSBW in the basin (P&J 2012), resulting in a net salinification across
360 most of the section (Fig 3o). Section A12 (0°E ; not shown), which cuts meridionally
361 through eastern end of the Weddell Gyre, is noisier than SR04, but roughly
362 consistent within errors with the pattern seen along SR04. Further to the east,
363 Section I06 (30°E) across the Enderby Basin shows water-mass freshening of less
364 than 0.1×10^{-3} PSS-78 yr^{-1} , smaller than the measurement error, but again
365 consistent with other lines in this basin, along with a compensating heave of $\sim 0.2 \times$
366 10^{-3} PSS-78 yr^{-1} (not shown). Together, these three lines yield a basin-mean
367 salinification of 0.1×10^{-3} PSS-78 yr^{-1} , significantly different from zero at 95%
368 confidence for $-0.2 < \theta < 0.5^\circ\text{C}$ (Fig. 4a).

369 North of the Weddell-Enderby Basin, the Scotia Sea and the Argentine Basin,
370 both fed by AABW from the Weddell Sea and vicinity (Fig. 1), show little bottom
371 water salinity change rising above the noise. SR01 across Drake Passage (not
372 shown) is extremely noisy and we can find no discernable signal. All sections
373 crossing the Argentine Basin shows little water-mass change but a slight
374 salinification owing to deep isotherm heave (not shown).

Finally, the basin-mean $d\theta/dt$ for all three of the southernmost basins exhibits statistically significant warming trends ranging from $0.002\text{--}0.005\text{ }^{\circ}\text{C yr}^{-1}$ for $\theta < 0.5\text{ }^{\circ}\text{C}$ (Fig. 4g-i). This trend is comparable to the $0.003\text{ }^{\circ}\text{C yr}^{-1}$ warming P&J (2010) found below 3000 m south of the SAF, only here we have averaged along depths of mean potential isotherms within each basin instead of on isobaths as done in P&J (2010). The basin-mean $d\theta/dt$ is more consistent along depth of mean isotherms (Fig. 4g-i vs. P&J (2010) Fig. 9d), arguably making this new calculation the preferable method.

5. Freshwater, heat, and SLR budgets

Here we apply the basin means (Fig. 4) for water-mass, heave, total S, and θ trends over the entire Southern Ocean, here defined as south of 30°S , to evaluate their contributions to ocean freshwater budgets (Section 5a), global heat budgets (Section 5b), and SLR (Section 5c). For basins and the entire domain, the budget calculations are conducted from the bottom to three upper bounds: climatological $\theta = 0\text{ }^{\circ}\text{C}$ as a rough proxy for the upper boundary of AABW (Foster and Carmack, 1976), 4000 m for a deep ocean estimate where water properties are most strongly influenced by AABW (Johnson 2008; following P&J 2010), and 2000 m to extended our analysis to the current maximum sampling depth of Argo floats (e.g. Roemmich et al. 2009).

The basin-mean rates and errors are applied to the climatological θ and S fields (Gouretski and Koltermann 2004). The climatological θ and S vertical profiles are put onto a uniform 20-m depth grid using a shape-preserving piecewise cubic

interpolation. Each basin-mean rate and its standard deviation on the θ -grid (Fig. 4) are interpolated onto the climatological θ profiles at each horizontal gridpoint, assigning all four rates and their standard deviations as discussed above. Regions above the CDW θ maximum are not considered here since the method used does not allow it. Given the focus on AABW changes, this limitation is minor.

a. Freshwater budget:

Here we quantify the fresh water uptake owing to deep water-mass changes in the deep Southern Ocean, including in AABW, and compare its magnitude to that of the excess mass flux off Antarctica in recent decades from ice melt. We estimate the freshwater flux by calculating the amount of freshwater (V_{fw}) necessary to add to an initial volume (V_i) with initial salinity (S_i) in order to cause the water to freshen at the observed dS_{WM}/dt over a 1-year period to a final salinity (S_f). If salt is conserved and we only change the salinity by adding freshwater to the system to change V_i to a final volume (V_f), then V_{fw} is calculated as:

$$V_{fw} = \int V_f - V_i = \int \left(\frac{S_i}{S_f} - 1 \right) \cdot dv, \quad (1)$$

neglecting the relatively small change in density. Here S_i is the gridded climatological salinity (Gouretski and Koltermann 2004) and S_f is calculated by applying dS_{WM}/dt for one year at each climatological grid point. The dv for each grid point is calculated as the volume of the half-degree longitude by a half-degree latitude by 20-m depth box. Local freshwater fluxes in $m \text{ yr}^{-1}$ are found by integrating in the vertical from the bottom upwards to $\theta = 0^\circ\text{C}$, 4000 m, and 2000 m

(Fig 5) and basin totals by integrating over the whole basin below these same surfaces (Table 1). The standard deviations of V_{fw} for the basin means are found by applying $S_f \pm$ one standard deviation of S_f in (1). The basin DOFs are θ volume-weighted mean along-isotherm DOFs below a given surface (Fig. 4) and the 95% confidence intervals (Table 1) are calculated using Student's t-distribution. Finally, a total for the whole Southern Ocean below each top surface is calculated as a sum of all the basin values south of 30 °S with 95% confidence intervals found using the sum of the basin standard deviations and DOFs (Table 1). Again, the 95% confidence intervals reflect the spatial variance of the trend estimates, and assume that the along-section variability in each basin is representative of that within the entire basin (Table 1).

Local estimates from the bottom to $\theta = 0$ °C show the largest deep freshening occurring in the west Pacific and Indian Ocean sectors (Fig. 5). The local freshwater flux in these regions for $\theta = 0$ °C exceeds 0.02 m yr⁻¹ over the north-west corner of the Amundsen–Bellingshausen Basin and most of the deep portions of the Australian-Antarctic Basin (Fig. 5a), despite $\theta < 0$ °C occupying only ~1000–1500 m of the water column. This flux is equivalent to total freshwater additions of 25 ± 9 and 48 ± 36 Gt yr⁻¹ into the Amundsen-Bellingshausen and Australian-Antarctic basins, respectively (Table 1), suggesting that a large fraction of the estimated recent 140 Gt yr⁻¹ freshwater flux from ice melt (Rignot et al. 2008) may be taken up by freshening AABW.

The Weddell-Enderby Basin also shows a slight freshwater flux of 0.005 m yr⁻¹ below $\theta = 0$ °C (Fig.5). This small amount reflects the very slight observed 0.1×10^{-1}

³ PSS-78 yr⁻¹ water-mass freshening (Fig. 4a) applied to the relatively large volume of AABW, with water of $\theta \leq 0$ °C isotherm as much as 4000 m in thickness (e.g. Fig. 3m). The relatively large volume of AABW combined with the small water-mass freshening, gives an uncertain total freshening of 24 ± 54 Gt yr⁻¹.

Integrating vertically to 4000 and 2000 m further emphasizes the pattern discussed above south of the SAF and shows a strong water-mass salinification in the NADW north of the SAF at intermediate depths (Fig. 5, Table 1). Integrating to 4000 m, containing only a fraction of $\theta < 0$ °C (Fig. 3; bold black contours), gives a fraction the freshening seen for $\theta < 0$ °C (Fig. 5b). Integrating to 2000 m (Fig. 5c), the local water-mass freshwater flux south of the SAF is almost identical as that from integrating to the 0 °C isotherm, indicating that water-mass freshwater changes are mostly constrained to $\theta < 0$ °C with little water-mass freshening in the waters between 0 °C and 2000 m (Fig. 3a,d,g,j). South of the SAF 2000 m lies below CDW entering from the north, therefore, none of these isotherms or isobar surfaces reflect changes in CDW south of the SAF. However, north of the SAF between 2000 and 3000 m, in the waters heavily influenced by NADW ($\theta \sim 2.8$ °C) a strong salinification is observed, seen as a negative local fresh water fluxes of between -0.01 and -0.1 m yr⁻¹ in the local fluxes (Fig 5c). These waters are also freshening and warming from heave (not shown). The property changes in these regions are separate from the deep AABW changes discussed in this paper, and likely indicate physical changes in the NADW in these regions.

b. Heat budget

We find large and statistically significant heat uptake in each basin and the whole Southern Ocean for $\theta < 0^\circ\text{C}$, below 4000 m, and below 2000 m (Table 1). The rate of heat gain (Q) is given by

$$Q = \int \rho \cdot C_p \cdot \frac{d\theta}{dt} \cdot dv, \quad (2)$$

where density (ρ) and heat capacity (C_p) are calculated from the climatological θ , S , and pressure at each grid point. The standard deviation of Q is found by replacing $d\theta/dt$ in (2) with the standard deviations of $d\theta/dt$. We sum the errors because the individual grid points are not independent of each other. The total DOF and 95% confidence intervals for each basin and total Southern Ocean (Table 1) are estimated by previously described methods (Section 5a). We find a large, statistically significant, heat gain throughout the water column in the Southern Ocean. Totals found here are slightly smaller than P&J 2010 (discussed further in Section 6), but agree within uncertainties.

c. Sea Level Rise

Changes in density of AABW owing to dS_T/dt , dS_{WM}/dt , dS_H/dt and $d\theta/dt$ contribute to halosteric and thermosteric SLR. We calculate the contribution of each component to SLR using:

$$SLR_{halosteric} = \frac{\int -\beta \cdot \frac{dS}{dt} \cdot dv}{SA} \text{ and } SLR_{thermosteric} = \frac{\int \alpha \cdot \frac{d\theta}{dt} \cdot dv}{SA}, \quad (3)$$

where the thermal expansion coefficient, α , and the haline contraction coefficient, β , are calculated locally from the climatological gridded θ , S , and pressure. For a local estimate, the integral is evaluated vertically from the bottom to a top surface at each

grid point where the surface area (SA) has the surface area of that grid point, yielding its contribution to local SLR in mm yr^{-1} (Fig. 6). Again, the top surfaces considered here are $\theta = 0^\circ\text{C}$, 4000 m, and 2000 m. For each basin an average SLR is calculated using (3) where the volume integral is now over the entire region from the bottom to the top surface under consideration, and SA is the surface area of that top surface for the basin (Table 1). The gridded standard deviations are integrated again using (3) to estimate the total basin standard deviation. The 95% confidence intervals are estimated assuming Student's t-distribution and using the total DOF below a given surface as described in Section 5a.

Water-mass freshening tends to reduce SLR in all three southernmost basins while the heave salinification raises SLR (Fig. 6). The local effects of water-mass freshening vary spatially, but follow the spatial patterns seen in the freshwater flux (Fig. 5), with the strongest signal seen in the South Pacific and South Indian (Fig. 6a,e,i). Heave salinification counteracts some of the SLR, except in the Amundsen-Bellingshausen Basin where S is almost constant versus θ in deeper, colder waters (Fig. 6b,f,j; Table 1). The net effect is a slight ($\sim -0.02 \text{ mm yr}^{-1}$) local negative SLR in the South Atlantic and a net positive ($\sim 0.03 \text{ mm yr}^{-1}$) SLR in the South Pacific and South Indian sectors of the Southern Ocean (Fig. 6c,g,k; Table 1). In total, the Southern Ocean salinity changes have a near-zero net effect on SLR (Table 1), owing to the contribution of salinification in the Weddell-Enderby and Argentine basins almost exactly canceling the contribution of freshening in Australian-Antarctic and Amundsen-Bellingshausen basins. The salinity contribution is smaller than the

warming contribution of 1–2 mm yr⁻¹ throughout the Southern Ocean (Fig. 6d,h,l;
Table 1).

6. Discussion

The Southern Hemisphere has experienced dramatic changes in recent decades owing to increases in atmospheric concentration of greenhouse gases and ozone-depleting chemicals. These changes include increased Southern Ocean warming (Gille 2008), increased glacial melt in the East Antarctic and Antarctic Peninsula (Rignot et al. 2008), a global slowdown of the bottom limb of the MOC (Kawano et al. 2010, Kouketsu et al. 2011; P&J 2012), and freshening of AABW (Jacobs and Guilivi 2010, Swift and Orsi 2012). Here we have examined property changes in the deep Southern Ocean, distinguishing between changes in the θ -S relation and vertical heave of θ surfaces within and associated with AABW. We conclude with a discussion comparing the amount of warming and freshening estimated in AABW to the global radiative imbalance, total glacial meltwater runoff from Antarctica, and global mean SLR.

Freshening of AABW in the Pacific and Indian sectors of the deep Southern Ocean appears to accounts for roughly half of the net Antarctic continental ice melt of recent years. The strongest freshening owing to water-mass shifts is seen near the AABW source regions and follows the path of AABW deep circulation in the three southernmost basins (Fig. 5a) reflecting the advection of a fresher variety of AABW into the deep Southern Ocean. The strongest freshening signal in the youngest AABW waters to the south with no freshening observed in the older AABW

further to the north (Fig. 5) suggests that this freshening flux may have started relatively recently. The Amundsen coast freshwater flux into the South Pacific and South Indian oceans that freshens the shelf water components of AABW there is probably largely owing to net continental ice melt (Jacobs and Guilivi 2010), estimated to be 140 Gt yr^{-1} over recent decades (Rignot et al. 2008). Our estimates are that the deep Amundsen-Bellingshausen and Australian-Antarctic basins have exhibited increases of 25 ± 9 and $48 \pm 36 \text{ Gt yr}^{-1}$, respectively, of fresh water between roughly 1991 and 2008, making the deep ocean a significant sink for the recent increase in glacial melt. The Weddell Basin also exhibits hints of water-mass freshening, albeit at a slower rate that is smaller than the measurement error. However, the spatial pattern of strongest freshening in the newest AABW and the consistency of the freshening throughout the basin (Fig. 3m) suggest that Weddell AABW may also be getting fresher.

The heave component of AABW changes found here reflects a loss of volume in AABW over time, seen farther from the source than the advected water mass freshening signal because production rate changes are communicated by pressure waves on much shorter time scales (e.g., Masuda et al. 2010). P&J (2012) found an 8 SV loss in volume of deep Southern Ocean water colder than 0°C , suggesting a recent decrease in the production of AABW. Paleoproxies indicate that the bottom limb of the MOC has been in multiple steady states during different climate regimes (Lynch-Stieglitz et al. 2007). Current water-mass volumes and chemistry of the global inventory of AABW vs. NADW suggest that past rates of AABW production may have been higher, also supporting the hypothesis of smaller production rates of AABW in

recent decades (Broecker et al. 1999; Johnson 2008). Here we separate heave from water-mass changes in the deep ocean and show that while the water-mass changes are currently limited to the deep basins adjacent to Antarctica, heave is responsible for part of the deep ocean changes there, and most, if not all, of the deep ocean changes in AABW further north. Furthermore, the deep volume loss of water colder than 0 °C is consistent with the warming and salinification of the water between 0 °C isotherm and 1000 m in the South Indian and South Pacific oceans (Fig. 3b,e,h,k,n).

Further investigation of the relative contribution of heave verses water-mass changes in AABW, including the source of the freshening, could be conducted using chemical tracers such as oxygen, nutrients, $\delta^{18}\text{O}$, and chlorofluorocarbons along repeated sections. Temporal changes in these chemical tracers would provide additional information about changes in the age, water-properties, and formation rates of the AABW. High-resolution models could also be used to examine the possible mechanisms of AABW changes. However, ocean global circulation models (OGCMs), such as those used for climate projections, do not yet resolve the complex set of processes involved in AABW formation and thus are not yet likely to reproduce accurately observed AABW changes.

AABW warming from heave contributes to the net ocean heat uptake. Earth is currently out of radiative balance owing to increasing atmospheric greenhouse gas concentrations. Satellite and in situ measurements show that Earth has been gaining heat at a rate of 183 TW between 1972 and 2008 (Church et al. 2011) with 90% of the excess energy being absorbed by the ocean. For comparison, the 33.8 ± 3.1 TW of warming found here south of 30°S below 2000 m (Table 1) amounts to

about $0.07 \pm 0.01 \text{ W m}^{-2}$ when calculated as a flux over the entire Earth surface. This is about 14% of the above total heat uptake.

The values of heat gain we find in the Southern Ocean are generally smaller than those of P&J (2010), and have smaller confidence intervals. Our mean heat fluxes below 4000 m in the Amundsen-Bellinghousen, Australian-Antarctic, and Weddell-Enderby basins are 0.14 ± 0.05 , 0.11 ± 0.07 , and $0.23 \pm 0.10 \text{ W m}^{-2}$, respectively.

Comparable values from P&J (2010) are 0.20 ± 0.14 , 0.32 ± 0.17 , and $0.44 \pm 0.36 \text{ W m}^{-2}$, respectively. These two sets of estimates agree within confidence limits. While some data have been added for the most recent estimates, much of the difference is owing to a change in methods. We now find basin means on mean θ depths and apply them by θ to the climatological mean θ field instead of doing calculations on isobars. This new method gives smaller heat gains than P&J (2010) because the large warming in the deep southernmost waters raises the whole basin mean along an isobar, thus raising the basin total when integrated on isobars. When the rates are calculated and applied on θ , the strongest signal is contained geographically to the deep southernmost region, thus giving a more accurate, but smaller total heat flux. The 95% confidence intervals are slightly smaller here than in P&J (2010) partly because we use more data, but mostly because the variations across the basin are smaller on mean depths of isotherms than along isobars.

Finally, both the observed heave and water-mass freshening signals in the deep Southern Ocean contribute to SLR (Table 1). Global mean sea level is estimated to rise at a rate of $3.2 \pm 0.4 \text{ mm yr}^{-1}$ between 1993 and 2008, with $0.7 \pm 0.3 \text{ mm yr}^{-1}$ owing to thermal expansion in the upper water column and the rest owing to ice

melt, terrestrial water storage changes, and deep ocean warming (Church et al. 2011). Water property changes south of 30°S for $\theta < 0$ °C cause a local mean SRL of 0.52 ± 0.18 mm yr⁻¹ with almost all of this owing to changes in θ (Table 1). The heave component, comprised of the sum of +0.52 mm yr⁻¹ SLR owing to warming and -0.08 SLR mm yr⁻¹ from salinification heave (Table 1), accounts for a SLR of +0.44 mm yr⁻¹. The water-mass freshening causes an additional 0.09 mm yr⁻¹. Therefore, in the deep Southern Ocean, local SLR owing to AABW changes are a significant fraction of the global mean rate of SLR.

Acknowledgments:

We thank the hundreds of people who helped to collect, calibrate, process, and archive the WOCE and CLIVAR data sets, without whom global assessments of ocean variability like this one would be impossible. We also thank those who provided us with unreported SSW batch numbers for many cruises. D. Roemmich suggested an improvement for the error analysis. Finally, suggestions of two anonymous reviewers and editor Anand Gnanadesikan improved this manuscript. This work was supported by the NOAA Climate Program Office, NOAA Research, and NASA Headquarters under the NASA Earth and Space Fellowship Program - Grant NNX11AL89H.

APPENDIX

Ad-hoc Salinity Adjustments

We attempt to correct for small intercruise salinity biases as offsets for all occupations of repeated hydrographic sections (Table A1; see P&J 2012 for full data set description). We estimate these offsets by comparing S data in select geographical regions containing old, well-mixed, low-variability water, where the adjective old denotes a long time since the water was last in contact with the atmosphere. These small intercruise S biases can arise from differences in sampling, measuring, and calibration routines conducted by different personnel.

Intercruise S offsets are identified for all occupations of every section. First, each cruise is divided into subsections based on topographic and dynamic boundaries (such as fronts). Areas near boundaries, strong currents, or water-mass fronts are excluded. For each occupation at each location along a section, the S data are linearly interpolated onto to a 0.01 °C resolution θ -grid. The intercruise difference in S, ΔS , is calculated at each θ and each location along the section by subtracting the mean S of all the co-located occupations from each individual occupation. A mean (ΔS_{mean}) and variance (ΔS_{var}) are calculated for each subsection along θ surfaces. Within each subsection, a 0.1 °C-thick layer is chosen balancing where ΔS_{var} is small and the waters are oldest, as determined by examination of the chlorofluorocarbon, oxygen, nitrate, and $\Delta^{14}\text{C}$ distributions for the WOCE occupation of each section using the WOCE Atlases (e.g., Orsi and Whitworth, 2005). These portions of the water column are chosen to maximize the likelihood that ΔS estimates are owing to cruise measurement biases, not physical changes. The

weighted means of ΔS_{mean} , $\Delta \bar{S}_{\text{mean}}$, within the selected isotherm bands are found using the inverses of ΔS_{var} for weights. Similarly, the weighted means of ΔS_{var} , $\Delta \bar{S}_{\text{var}}$, are found using ΔS_{var} as weights. Finally, the S offset for an entire cruise is calculated as the $\Delta \bar{S}_{\text{var}}$ weighted mean of $\Delta \bar{S}_{\text{mean}}$ (Table A1).

The global array of repeated hydrographic sections collected through WOCE and GOSHIP programs are considered here, consisting of 33 lines with a total of 146 legs collected between 1981 and 2012. SSW batches and their recommended SSW offsets (Kawano et al. 2006; T. Kawano personal comm. 2011) are noted along with the additional ad-hoc offset found here (Table A1). Offsets are added to salinity data to obtain the final value. SSW batch offsets are available for 91% of the legs, with missing values either because the SSW batch used is too new for an offset to be estimated or because the SSW batch used is unknown. Additional ad-hoc offsets are found for 87% of the legs, with the missing offsets owing to the leg length being too short or the absence of a location on the section suitable to identify an offset. Of the 132 net offsets, 118 are less than the stated CTD salinity accuracy of 0.002 PSS-78, with the mean magnitude of the offsets being 0.0008 PSS-78 (Fig A1). While the application of SSW batch offsets improves the agreement among occupations of each section, it does not eliminate the need for ad-hoc offsets to reduce intercruise salinity biases (Fig. A1).

While these offsets are small, they are important for sea level rise estimates. For example, a 0.002 PSS-78 increase in S applied a 1000-m of a 0°C, 34.6 PSS-78 column of water results in a 0.14 mm decrease in SLR compared to only a 0.03 mm SLR increase from a 0.002 °C increase in temperature. In addition, the observed

668 freshening between sequential cruises ~10 years apart, ranges from 0 to 1 order of
669 magnitude greater than the WOCE stated salinity accuracy but 1 to 2 orders of
670 magnitude greater than the WOCE temperature accuracy.

671

References

- Aoki, S., S. R. Rintoul, S. Ushio, S. Watanabe, and N. L. Bindoff, 2005: Freshening of the Adélie Land Bottom Water near 140°E. *Geophys. Res. Lett.*, **32**, L23601, doi:10.1029/2005GL024246.
- Church, J. A., N. J. White, L. F. Konikow, C. M. Domingues, J. G. Cogley, E. Rignot, J. M. Gregory, M. R. van den Broeke, A. J. Monaghan, and I. Velicogna, 2011: Revisiting the Earth's sea-level and energy budgets from 1961 to 2008. *Geophys. Res. Lett.*, **38**, L18601, doi:10.1029/2001GL048794.
- Coles, V. J., M. S. McCartney, D. B. Olson, and W. M. Smethie Jr., 1996: Changes in Antarctic Bottom Water properties in the western South Atlantic in the late 1980s. *J. Geophys. Res.*, **101**, 8957–8970.
- Bindoff, N.L., and T.J. McDougall, 1994: Diagnosing Climate Change and Ocean Ventilation using Hydrographic Data. *Journal of Physical Oceanography*, **24**, 1137-1152. ISSN 1520-0485.
- Broecker, W. S., S. Sutherland, and T. H. Peng, 1999: A possible 20th-century slowdown of Southern Ocean deep water formation. *Science* **286**, 1132-1135, doi:10.1126/science.286.5442.1132.
- Fahrbach, E., M. Hoppema, G. Rohardt, M. Schroder, and A. Wisotzki, 2004: Decadal-scale variations of water mass properties in the deep Weddell Sea. *Ocean Dynamics*, **54**, 77–91.
- Fahrbach E., M. Hoppema, G. Rohardt, O. Boebel, O. Klatt, and A. Wisotzki, 2011: Warming of deep and abyssal water masses along the Greenwich meridian on

693 decadal time scales: The Weddell gyre as a beat buffer. *Deep-Sea Res. II*, **58**,
694 2508–2523, doi:10.1016/j.dsr2.2011.06.007.

695 Foster, T. D., and Carmack, E. C., 1976: Frontal zone mixing and Antarctic Bottom
696 Water formation in the southern Weddell Sea. *Deep-Sea Res.*, **23**, 301–317.

697 Fukasawa, M., H. Freeland, R. Perkins, T. Watanabe, H. Uchida, and A. Nishima, 2004:
698 Bottom water warming in the North Pacific Ocean. *Nature*, **427**, 825–827.

699 Gille, S. T., 2008: Decadal-scale temperature trends in the Southern Hemisphere
700 ocean. *J. Climate*, **21**, 4749–4765.

701 Gordon, A. L., 1972: Spreading of Antarctic Bottom Waters, II In: *Studies in Physical*
702 *Oceanography - A Tribute to George Wust on His 80th Birthday*. A.L. Gordon (ed),
703 Gordon and Breach, Science Publ., N.Y.: 1-17.

704 Gordon A. L., B. Huber, D. McKee, and M. Visbeck, 2010; A Seasonal cycle in the
705 export of bottom water from the Weddell Sea. *Nature Geoscience*, **3**, 551-556,
706 doi:10.1038/ngeo916.

707 Gouretski, V. V., and K. P. Koltermann, 2004: *WOCE Global Hydrographic Climatology*.
708 Berichte des bundesamtes für seeshiffahrt und hydrographie, 35, pp. 52+2 CD-
709 ROMs.

710 Jacobs, S. S., 2004: Bottom water production and its links with the thermohaline
711 circulation. *Antarctic Science*, **4**, 427-437, doi:10.1017/S095410200400224X.

712 Jacobs, S. S., and C. F. Giulivi, 2010: Large multi-decadal salinity trends near the
713 Pacific-Antarctic Continental Margin. *J. Climate*, **23**, 4508–4524,
714 doi:10.1175/2010JCLI3284.1.

715 Johnson, G. C., 2008: Quantifying Antarctic Bottom Water and North Atlantic Deep
 716 Water volumes. *J. Geophys. Res.*, **113**, C05027, doi:10.1029/2007JC004477.
 717 Johnson, G. C., and S. C. Doney, 2006: Recent western South Atlantic bottom water
 718 warming. *Geophys. Res. Lett.*, **33**, L14614, doi:10.1029/2006GL026769.
 719 Johnson, G. C., S. Mecking, B. M. Sloyan, and S. E. Wijffels, 2007: Recent bottom water
 720 warming in the Pacific Ocean. *J. Climate*, **20**, 5365–5375.
 721 Johnson, G. C., S. G. Purkey, and J. L. Bullister, 2008: Warming and freshening in the
 722 abyssal southeastern Indian Ocean. *J. Climate*, **21**, 5353–5365.
 723 Joyce, T. M., 1991: Introduction to the collection of expert reports compiled for the
 724 WHP Program. WOCE Hydrographic operations and methods. WOCE Operations
 725 Manual. WHP Office Report WHPO-91-1, WOCE Report 68/91.
 726 Kawano, T., M. Aoyama, T. Joyce, H. Uchida, Y. Takatsuki, and M. Fukasawa, 2006:
 727 The latest batch-to-batch difference table of standard seawater and its
 728 application to the WOCE onetime sections. *J. Oceanogr.*, **62**, 777-792.
 729 Kawano, T., T. Doi, H. Uchida, S. Kouketsu, M. Fukasawa, Y. Kawai, and K. Katsumata,
 730 2010: Heat content change in the Pacific Ocean between the 1990s and 2000s.
 731 *Deep-Sea Res. II*, **57**, 1141–1151, doi:10.1016/j.dsr2.2009.12.003.
 732 Kouketsu, S., and Coauthors, 2011: Deep ocean heat content changes estimated from
 733 observation and reanalysis product and their influence on sea level change. *J.*
 734 *Geophys. Res.*, **116**, C03012, doi:10.1029/2010JC006464.
 735 Lumpkin, R., and K. Speer, 2007, Global ocean meridional overturning. *J. Phys.*
 736 *Oceanogr.*, **37**, 2550–2562.

737 Lynch-Stieglitz, J., and Coauthors, 2007: Atlantic meridional overturning circulation
 738 during the last glacial maximum. *Science*, **316**, 66–69,
 739 doi:10.1126/science.1137127.

740 Masuda, S., and Coauthors, 2010: Simulated rapid warming of abyssal North Pacific
 741 water. *Science*, **329**, 319–322, doi:10.1126/science.1188703.

742 McDonagh E. L., H. L. Bryden, B. A. King, R. J. Sanders, S. A. Cunningham, and R.
 743 Marsh, 2005: Decadal changes in the south Indian Ocean thermocline. *J. Climate*,
 744 **18**, 1575-1590.

745 Meredith, M. P., A. C. Naveira Garabato, A. L. Gordon, and G. C. Johnson, 2008:
 746 Evolution of the deep and bottom water of the Scotia Sea, Southern Ocean,
 747 during 1995–2005. *J. Climate*, **21**, 3327–3343.

748 Orsi, A. H. , T. Whitworth II, Hydrographic Atlas of the World Ocean Circulation
 749 Experiment (WOCE). Volume 1: Southern Ocean (eds. M. Sparrow. P. Chapman
 750 and J. Gould), International WOCE Project Office, Southampton, U.K., ISBN 0
 751 904175-49-9. 2005.

752 Orsi, A. H., G. C. Johnson, and J. L. Bullister, 1999: Circulation, mixing and production
 753 of Antarctic Bottom Water. *Prog. Oceanogr.*, **43**, 55–109.

754 Purkey, S. G., and G. C. Johnson, 2010, Warming of global abyssal and deep Southern
 755 Ocean waters between the 1990s and 2000s: Contributions to global heat and
 756 sea level rise budgets. *J. Climate*, **23**, 6336–6351. doi:10.1175/2010JCLI3682.1.

757 Purkey, S. G. and G. C. Johnson, 2012: Global contraction of Antarctic Bottom Water
 758 between 1980s and 2000s. *J. Climate*, **25**, 5830–5844. doi:10.1175/JCLI-D-11-
 759 00612.1

760 Rignot, E., J. L. Bamber, M. R. van Den Broeke, C. Davis, Y. Li, W. Jan Van De Berg, and
 761 E. van Meijgaard, 2008: Recent Antarctic ice mass loss from radar interferometry
 762 and regional climate modeling. *Nature Geoscience*, **1**, 106–110,
 763 doi:10.1038/ngeo102.

764 Rignot E., and S. S. Jacobs, 2002: Rapid bottom melting widespread near Antarctic
 765 ice sheet grounding lines. *Science*, **296**, 2020-2023,
 766 doi:10.1126/science.1070942.

767 Rintoul, S. R., 2007: Rapid freshening of Antarctic Bottom Water formed in the
 768 Indian and Pacific oceans. *Geophys. Res. Lett.*, **34**, L06606,
 769 doi:10.1029/2006GL028550.

770 Robertson R., M. Visbeck, A. L. Gordon, and E. Fahrbach, 2002: Long-term
 771 temperature trends in the deep waters of the Weddell Sea. *Deep-Sea Res. II*, **49**,
 772 4791–4806.

773 Roemmich, D., G. C. Johnson, S. Riser, R. Davis, J. Gilson, W. B. Owens, S. L. Garzoli, C.
 774 Schmid, and M. Ignaszewski. 2009. The Argo Program: Observing the global
 775 oceans with profiling floats. *Oceanography*, **22(2)**, 34-43.

776 Shepherd, A., D. J. Wingham, and J. A. D. Mansley, 2002: Inland thinning of the
 777 Amundsen Sea sector, West Antarctica. *Geophys. Res. Lett.*, **29**,
 778 doi:10.1029/2001GL014183.

779 Shepherd, A., D. Wingham, and E. Rignot, 2004: Warm ocean is eroding West
 780 Antarctic Ice Sheet. *Geophys. Res. Lett.*, **31**, L23402, doi:10.1029/2004GL021106.

781 Shimada, K., S. Aoki, K. I. Ohshima, and S. R. Rintoul, 2012: Influence of Ross Sea
 782 Bottom Water changes on the warming and freshening of the Antarctic Bottom

783 Water in the Australian-Antarctic Basin. *Ocean Sci.*, **8**, 419-432, doi: 10.5194/os-
 784 8-419-2012.
 785 Swift J. H., and A. H. Orsi, 2012: Sixty-four days of hydrography and storms: RVIB
 786 Nathaniel B. Palmer's 2011 S04P Cruise. *Oceanography*, **25(3)**, 54-55,
 787 doi:10.5670/oceanog.2012.74.
 788 Whitworth, T., III, 2002: Two modes of bottom water in the Australian-Antarctic
 789 Basin, *Geophys. Res. Lett.*, **29**, 1073, doi:10.1029/2001GL014282.
 790 Zenk, W., and E. Morozov, 2007: Decadal warming of the coldest Antarctic Bottom
 791 Water flow through the Vema Channel. *Geophys. Res. Lett.*, **34**, L14607,
 792 doi:10.1029/2007GJ030340.
 793

Table 1: Fresh water gain (FW; Gt yr⁻¹), Sea Level Rise (SLR; mm yr⁻¹) and heat uptake (TW) with uncertainties at the 95 % confidence level below $\theta = 0^\circ\text{C}$, 4000 m, and 2000m in the Amundsen-Bellingshausen Basin (ABB), Australian-Antarctic Basin (AAB), Weddell-Enderby Basin (WEB), and the whole Southern Ocean south of 30°S (Fig. 1). Freshwater estimates are calculated following (1) using basin mean freshening trends owing to only water-mass changes. Steric SLR trends are estimated from (3) broken into water-mass, heave, total salinity, and warming trends. The total steric SLR is also given. Heat uptake is calculated following (2) using basin mean warming trends. Values statistically different from zero at the 95% confidence are given in bold.

		FW (Gt yr ⁻¹)	SLR (mm yr ⁻¹)				Heat (TW)	
		Water-mass	Water-mass	Heave	Salinity	θ	Total	θ
Below 0 °C	ABB	25 ±9	0.17 ±0.06	0.00 ±0.02	0.18 ±0.07	0.31 ±0.10	0.49 ±0.13	1.0 ±0.5
	AAB	48 ±36	0.22 ±0.16	-0.07 ±0.05	0.15 ±0.18	0.5 ±0.28	0.65 ±0.33	2.5 ±1.3
	WEB	24 ±54	0.05 ±0.11	-0.12 ±0.12	-0.07 ±0.12	0.66 ±0.45	0.59 ±0.46	7.7 ±2.8
	Total S of 30S	99 ±56	0.09 ±0.05	-0.08 ±0.04	0.00 ±0.06	0.52 ±0.17	0.52 ±0.18	14 ±3
Below 4000m	ABB	9 ±4	0.03 ±0.01	-0.01 ±0.01	0.02 ±0.02	0.18 ±0.06	0.20 ±0.06	1.1 ±0.4
	AAB	17 ±13	0.12 ±0.1	-0.02 ±0.03	0.11 ±0.1	0.14 ±0.13	0.25 ±0.17	0.4 ±0.2
	WEB	10 ±28	0.03 ±0.09	-0.05 ±0.08	-0.02 ±0.05	0.30 ±0.23	0.28 ±0.24	1.9 ±0.8
	Total S of 30S	53 ±21	0.02 ±0.01	-0.02 ±0.01	0.01 ±0.01	0.13 ±0.05	0.14 ±0.05	5 ±1
Below 2000m	ABB	-28 ±43	-0.05 ±0.08	0.02 ±0.07	-0.03 ±0.08	0.44 ±0.26	0.41 ±0.27	5.7 ±1.8
	AAB	48 ±66	0.15 ±0.2	-0.12 ±0.21	0.03 ±0.29	1.03 ±0.83	1.06 ±0.89	8.1 ±3.5
	WEB	27 ±81	0.06 ±0.17	-0.13 ±0.19	-0.07 ±0.2	0.70 ±0.70	0.63 ±0.73	7.8 ±2.9
	Total S of 30S	-454 ±241	-0.12 ±0.06	0.09 ±0.07	-0.03 ±0.06	0.37 ±0.15	0.34 ±0.16	34 ±3

805 Table A1: IAPSO Standard Sea Water (SSW) batch number with recommended SSW
 806 batch salinity offset (Kawano et al. 2006; T. Kawano personal communication 2011)
 807 for each leg listed by WOCE ID (with alternative ID used on <http://cchdo.ucsd.edu> in
 808 parentheses if different) and year. If more than one leg of a section is occupied per
 809 year, legs are differentiated by geographical region (East (E), West (W), North (N),
 810 South (S), Central (C), or Antarctic (A)) or, if an exact repeat of a leg is done twice in
 811 one year, then legs are listed chronologically by the date of the first station occupied.
 812 If no SSW batch number is listed, we were unable to determine this information
 813 from cruise reports or through personal queries to data originators. As of
 814 September 2012, there is no known offset for batch numbers P113 and P152,
 815 therefore no SSW batch offset is applied for cruises using those SSW batches. The
 816 last column lists the additional ad-hoc salinity offsets estimated by and applied for
 817 our analyses (see Appendix). If legs do not have an ad-hoc salinity offset listed, then
 818 one was not possible to estimate owing to the section location or length. Both
 819 offsets are added to salinity data.

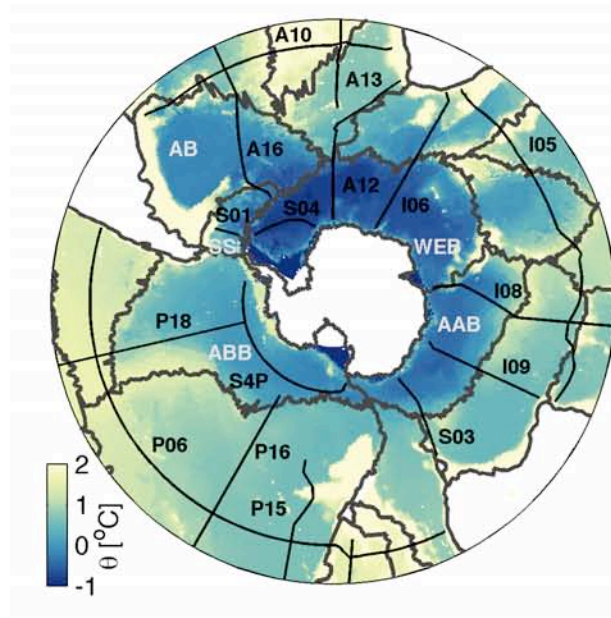
WOCE ID	yr	ssw batch number	ssw offset (x1000)	ad-hoc offsets (x1000)
A01(AR07)E	1990	P112	1.9	0.186
A01(AR07)W	1990	P104	1.1	N/A
A01(AR07)E	1991	P112/P114	1.9/2	N/A
A01E	1991	P112	1.9	-0.289
A01(AR07)E	1992	P119	0	-0.836
A01(AR07)W	1992	P112	1.9	N/A
A01(AR07)W	1993	P117	N/A	N/A
A01(AR07)E	1994	N/A	N/A	N/A
A01(AR07)W	1994	P123	0.7	N/A
A01W	1994	P124	0.6	-0.496
A01(AR07)E	1995	N/A	N/A	-0.551
A01W	1995	P126	0.6	N/A
A01(AR07)E	1996	N/A	N/A	1.870
A01(AR07)W	1996	P124	0.6	N/A
A01(AR07)E	1997	P129	0.4	N/A

A01(AR07)W	1997	P129	0.4	N/A
A01(AR07)W	1998	P133	0.3	N/A
A02	1994	P124	0.6	-1.849
A02	1997	P129	0.4	1.849
A05	1981	P93	0.9	-2.867
A05	1992	P120	-0.9	0.114
A05(AR01)	1998	P125	0.2	0.259
A05	2004	P143/P144	-0.2/-0.5	1.028
A05	2010	N/A	N/A	1.952
A10	1992	P120	-0.9	-1.110
A10	2003	P142	0.2	0.134
A10	2011	P152	N/A	0.829
A12	1992	P114	2	-0.553
A12(S04)	1996	P127	0.8	0.437
A12	1999	P134	0.3	-0.038
A12	2000	P135	0.2	0.624
A12	2002	P140	-0.3	-0.034
A12	2005	P144	-0.5	0.273
A13.5	1983	P92	-0.2	-1.276
A13.5	2010	P147	-0.5	1.276
A16N	1988	P108	1.7	0.587
A16C	1989	P108	1.7	-0.494
A16S	1989	P108	1.7	0.435
A16	1993	P119	0	-0.869
A16(A23)	1995	P125	0.2	0.332
A16(AR21)	1998	P133	0.3	0.166
A16	2003	P143	-0.2	-0.384
A16	2005	P143	-0.2	0.087
A16	2011	N/A	N/A	2.276
A20	1997	P131	0.1	-1.446
A20	2003	P140	-0.3	1.446
A22	1997	P131	0.1	-0.283
A22	2003	P140	-0.3	0.283
I02	1995	P128	1.4	0.246
I02	2000	P133/P138	0.3/-0.1	-0.246
I03	1995	P126	0.6	0.328
I03	2003	P142	0.2	-0.328
I04	1995	P126	0.6	-0.274
I04	2003	P142	0.2	0.274
I05	1987	P97	2.1	-1.406
I05W	1995	P126	0.6	0.836
I05E	1995	P126	0.6	0.449
I05	2002	P140	-0.3	1.031
I05	2009	P149	0.8	0.234
I06	1993	P121	0.4	-0.264
I06	1996	N/A	N/A	-0.042
I06	2008	N/A	N/A	0.186

I08S	1994	P124	0.6	-0.802
I08(I09N)N	1995	P126	0.6	0.479
I08	2000	P133/P138	0.3/-0.1	-0.564
I08(I09N)N	2007	P147	-0.5	0.206
I08S	2007	P147	-0.5	0.802
I09	1995	P124	0.6	-0.338
I09(S03)S	1995	P121/P123	0.4/0.7	N/A
I09	2004	P141	-0.3	0.338
IR6	1995	N/A	N/A	0.597
IR6	1995	N/A	N/A	0.828
IR6(I02)	2000	P133/P138	0.3/-0.1	-1.339
P01	1985	P96	2.5	1.154
P01C	1999	P135	0.2	-0.680
P01E	1999	P133/P134	0.3/0.3	0.386
P01H	1999	P135	0.2	N/A
P01W	1999	P133	0.3	-0.849
P01C	2007	P148	0.2	-0.304
P01W/E/H	2007	P148	0.2	-0.651
P02	1985	P96	2.5	0.956
P02E	1993	P123	0.7	1.175
P02	1994	P144	-0.5	-1.968
P02C	1994	P121	0.4	-2.600
P02W	1994	P144	-0.5	4.534
P02	2004	P144	-0.5	0.274
P03	1985	P96	2.5	1.764
P03E	2005	P145	-0.8	-1.553
P03W	2005	P145	-0.8	-2.009
P03	2006	P145	-0.8	N/A
P06C	1992	P116	1.4	-1.205
P06E	1992	P116	1.4	0.357
P06W	1992	P116	1.4	-1.167
P06W	2003	P142	0.2	0.358
P06E	2003	P142	0.2	-0.837
P06	2009	N/A	N/A	0.866
P09	1994	P123	0.7	-0.200
P09	2010	P152	N/A	0.200
P10	1993	P114/P120	2/-0.9	0.323
P10	2005	P145	-0.8	-0.323
P14	1992	P120	-0.9	0.087
P14	1993	P122	0.4	0.571
P14N	2007	P148	0.2	-0.777
P14S	2007	P148	0.2	-0.376
P15	1996	P114	2	-1.304
P15	2001	P140	-0.3	0.840
P15	2009	P148/P150	0.2/0.8	0.490
P16	1984	P92	-0.2	2.901
P16C	1991	P114	2	0.932

P16N	1991	P110	1.9	-1.431
P16S	1991	P108/P114	1.7/2	0.010
P16A	1992	P120	-0.9	0.222
P16S	2005	P144	-0.5	-0.319
P16N	2006	P145	-0.8	-1.141
P17S	1991	P108/P114	1.7/2	-0.512
P17C	1991	P120	-0.9	2.470
P17A	1992	P120	-0.9	0.460
P17N	1993	P122	0.4	0.915
P17	2001	P139	0.4	-1.754
P18S	1994	P114	2	-0.209
P18N	1994	P114	2	0.335
P18(AAIW)	2006	P146	-1.2	N/A
P18N	2007	P147	-0.5	-0.483
P18S	2008	P147	-0.5	0.209
P21W	1994	P123	0.7	-0.447
P21E	1994	P123	0.7	-0.240
P21	2009	P150	0.8	0.396
S01	1993	N/A	N/A	N/A
S01	1994	N/A	N/A	N/A
S01	1996	N/A	N/A	N/A
SR03	1991	P115	2.5	N/A
SR03	1993	P121	0.4	-5.643
SR03	1994	P121/P123/P137/P140	0.4/0.7/-0.4/-0.3	0.206
SR03(S03)	1995	P121/P123	0.4/0.7	-0.997
SR03	1995	P128/P130	1.4/0.3	3.454
SR03	1996	P128/P130	1.4/0.3	1.606
SR03	2001	P113/P133/P137/P140	N/A/0.3/-0.4/-0.3	1.385
SR03	2008	P140/P147/P148	-0.3/-0.5/0.2	0.884
S04	1989	P111	2.1	-0.703
S04	1990	P113	N/A	1.523
S04	1992	N/A	N/A	0.667
S04	1996	P127/P148	0.8/0.2	-1.893
S04	1998	P113	N/A	0.995
S04	2005	P144	-0.5	-0.716
S4P	1992	P108	1.7	0.059
S4P	2011	P152	N/A	-0.059

820

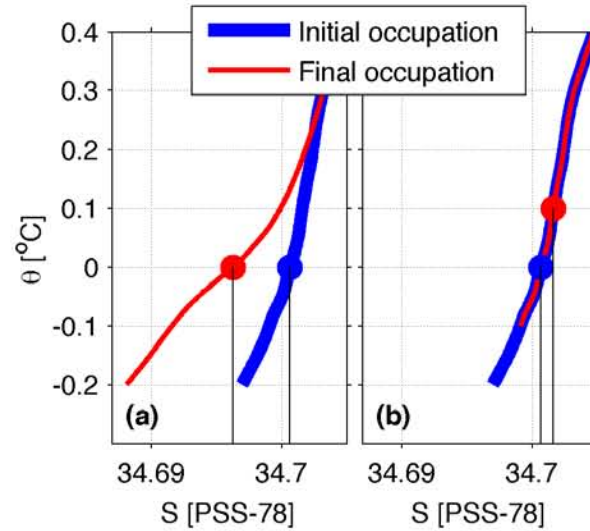


821

822 Fig. 1. Southern Ocean section locations (black lines) labeled with WOCE IDs (black
823 characters) and basin boundaries (gray lines) over bottom potential temperature
824 (color shading; Gourtski and Koltermann 2004) with land (white shading). Basin
825 names (white characters) are indicated by abbreviations including: Weddell-
826 Enderby Basin (WEB), Australian-Antarctic Basin (AAB), Amundsen-Bellingshausen
827 Basin (ABB), Scotia Sea (SS), and the Argentine Basin (AB).

828

829



829

830 Figure 2: Schematics of changes in salinity between an initial (blue) and final (red)

831 occupation of a given station owing to (a) water-mass change and (b) isotherm

832 heave. Water-mass changes (a) can be seen as a change in the θ -S curve causing a

833 deep freshening signal between occupations (black lines) at the same depths (dots).

834 Isotherm heave (b), caused by a vertical displacement of potential isotherms, causes

835 water at the same depth (dots) to warm and become more saline between

836 occupations (black lines).

837

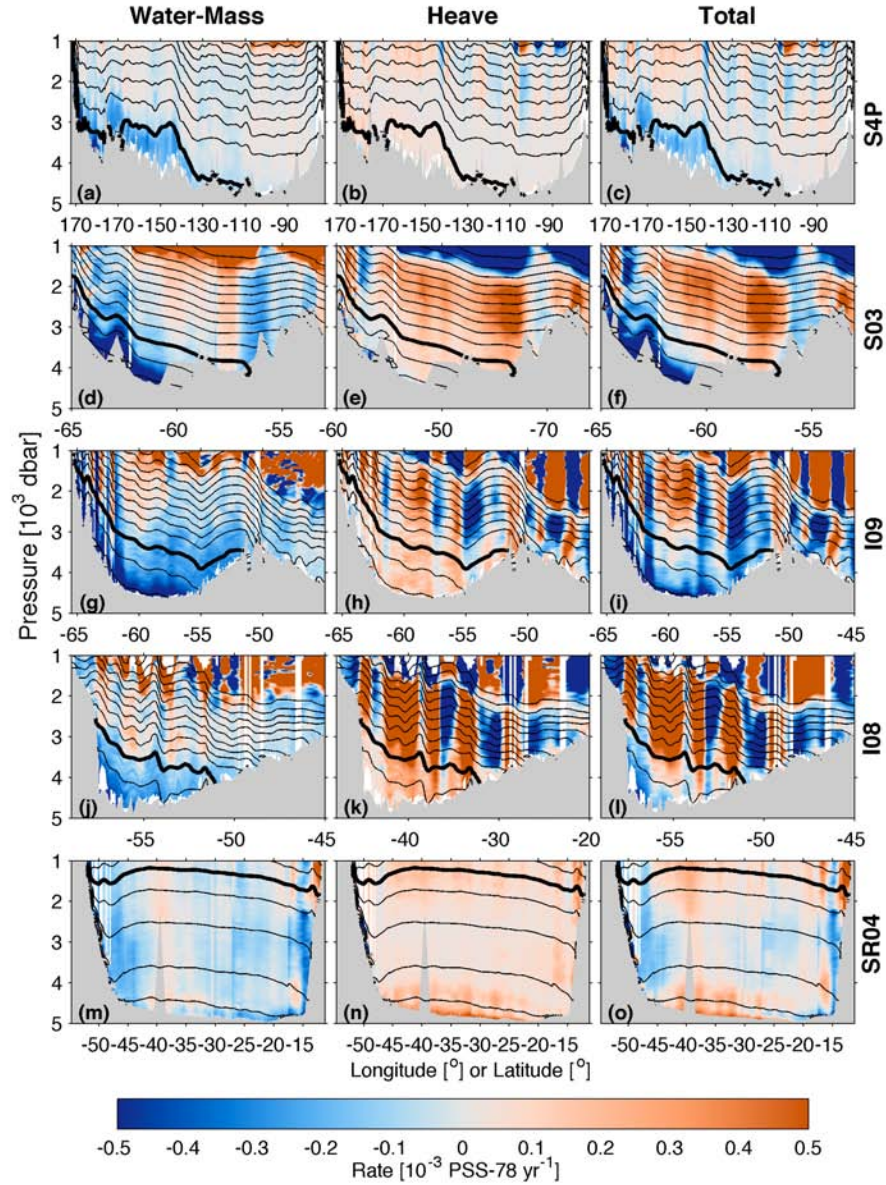
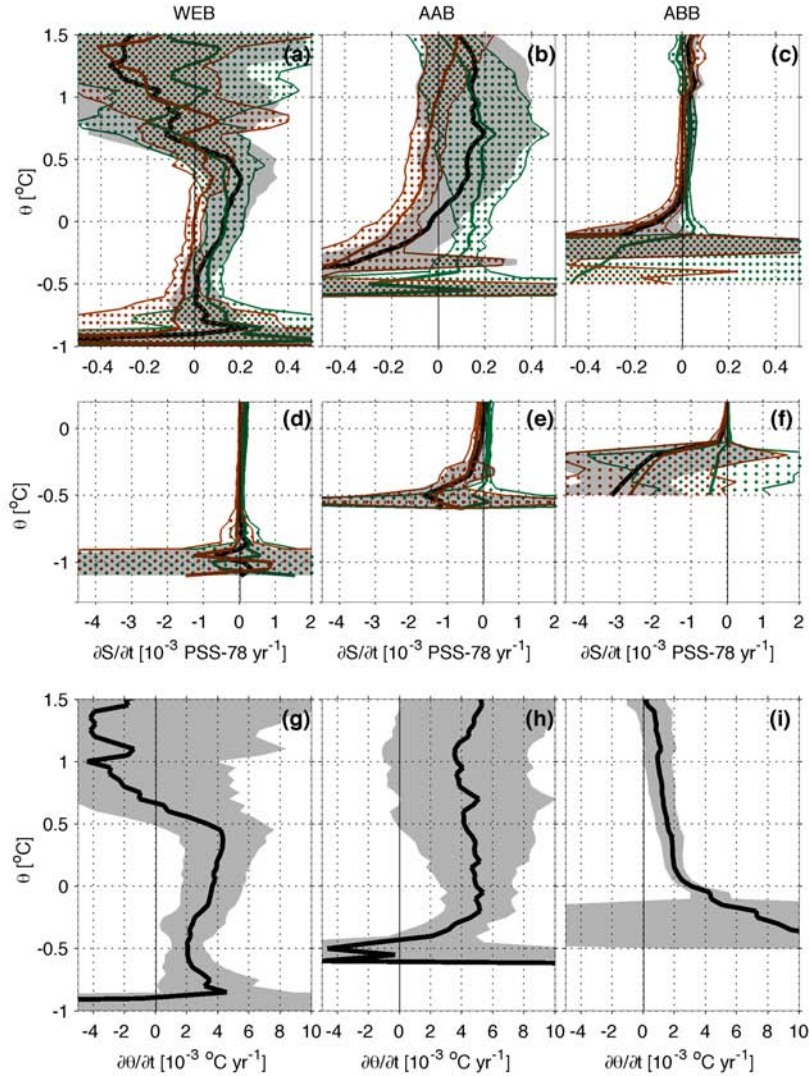


Fig. 3. Rate of change in S (color; in PSS-78 yr^{-1}) vs. pressure and latitude or longitude along S4P (a-c), S03 (d-f) across the Australian-Antarctic Basin, I09 (g-i) across the Australian-Antarctic Basin, I08 (j-l) across the Australian-Antarctic Basin, and SR04 (m-o) across the Weddell Sea (see Fig.1 for locations). Orange indicates areas of salinification and blue areas of freshening with mean isotherms contoured at $0.2\text{ }^{\circ}\text{C}$ intervals (thin black lines; 0°C isotherm thick black line). The water mass (a, d, g, j, m) and heave (b,e,h,k,n) contributions to the total (c,f,i,l,o) are separated.



845

846 Figure 4: Basin-mean rates of change in S (black; a–f; PSS-78 yr⁻¹) and θ (black g–i;

847 °C yr⁻¹) with 95% confidence intervals (gray shading) estimated along time-mean θ

848 surfaces in the Weddell-Enderby Basin (WEB), Australian-Antarctic Basin (AAB) and

849 Amundsen- Bellingshausen Basin (ABB). The water-mass (red) and heave (green)

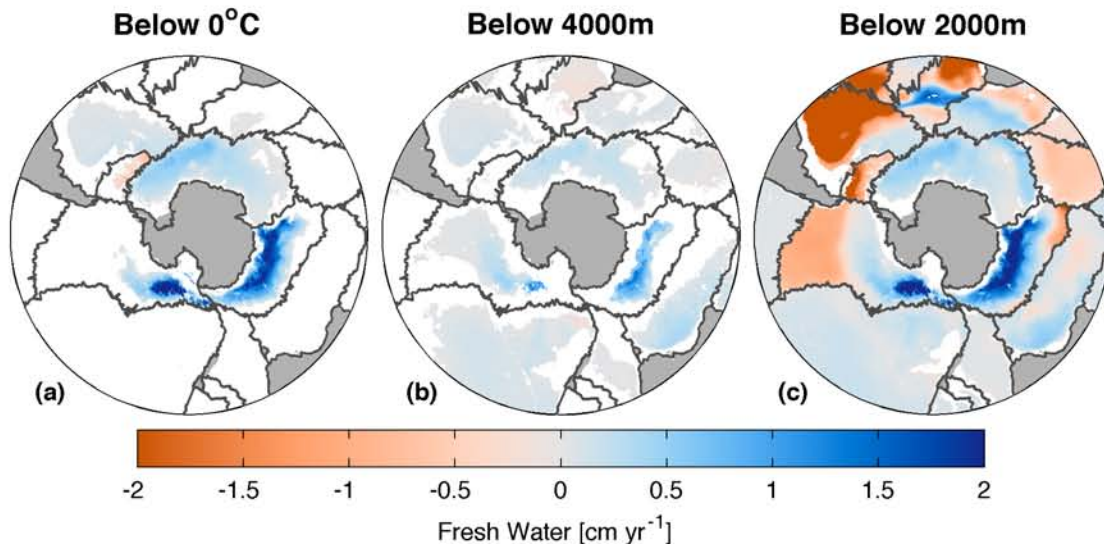
850 contributions to the total with 95% confidence intervals (dots) are shown over a

851 large θ range to show interior changes (a–c) as well as vertically expanded over a

852 limited θ range (d–f) to show large changes found in the coldest waters along the

853 continental slope (see Fig 3).

854



855

856 Figure 5. Local vertical column freshwater fluxes in cm yr^{-1} (color) below (a) 0°C , (b)

857 2000 m, and (c) 4000 m equivalent to observed water-mass salinity changes. Basin

858 boundaries (gray lines) and land (gray shading) are shown.

859

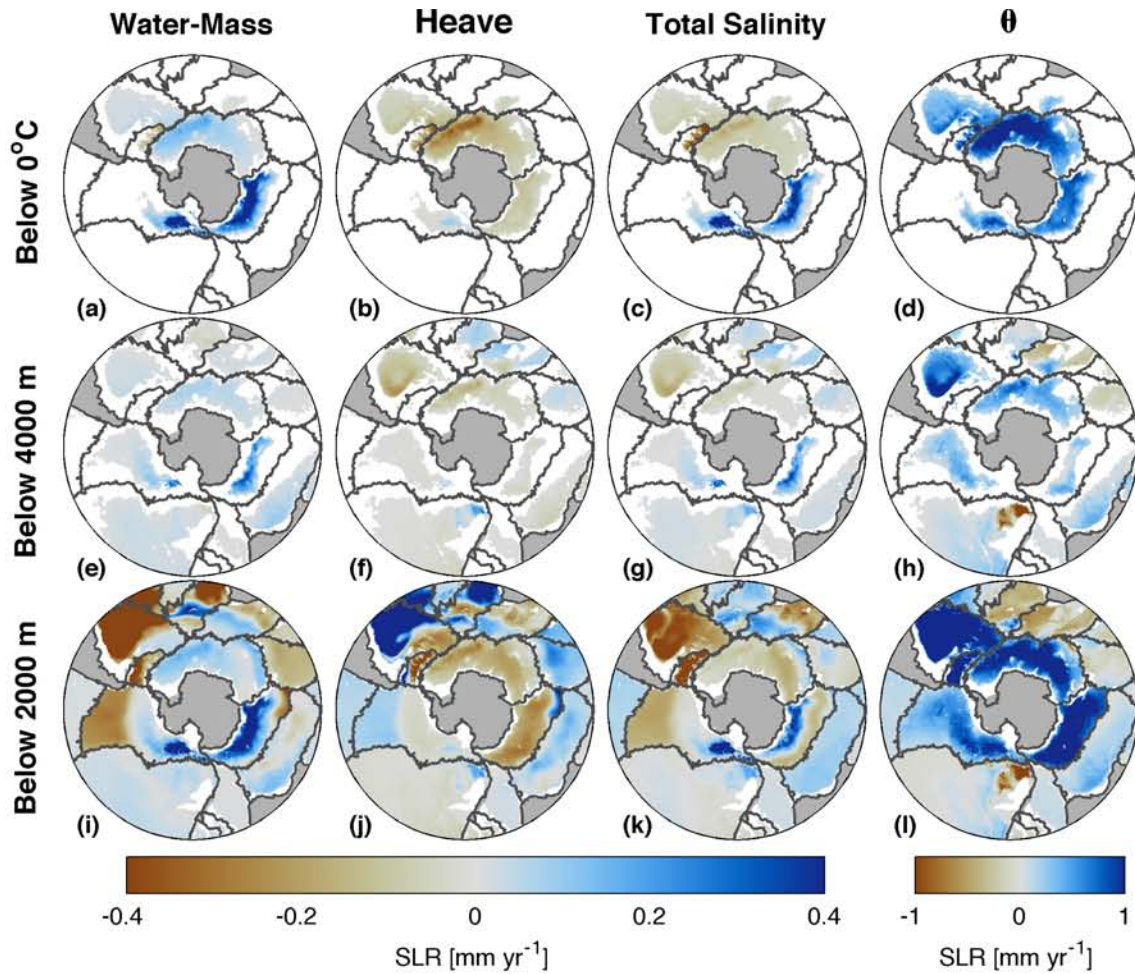


Figure 6: Vertical column total sea level rise [mm yr^{-1}] below $\theta = 0^\circ\text{C}$ (a–d), 4000 m (e–h), and 2000 m (i–l) owing to water-mass S changes (a,e,i), heave salinity changes (b,f,j), net salinity changes (c,g,k), and θ changes (d,h,l). Blue indicates areas of positive SLR and brown of negative SLR (see color legends). SLR is calculated based on basin (gray lines) mean rates of change in S and θ (e.g. Figure 4) along climatological isotherms (see Section 4).

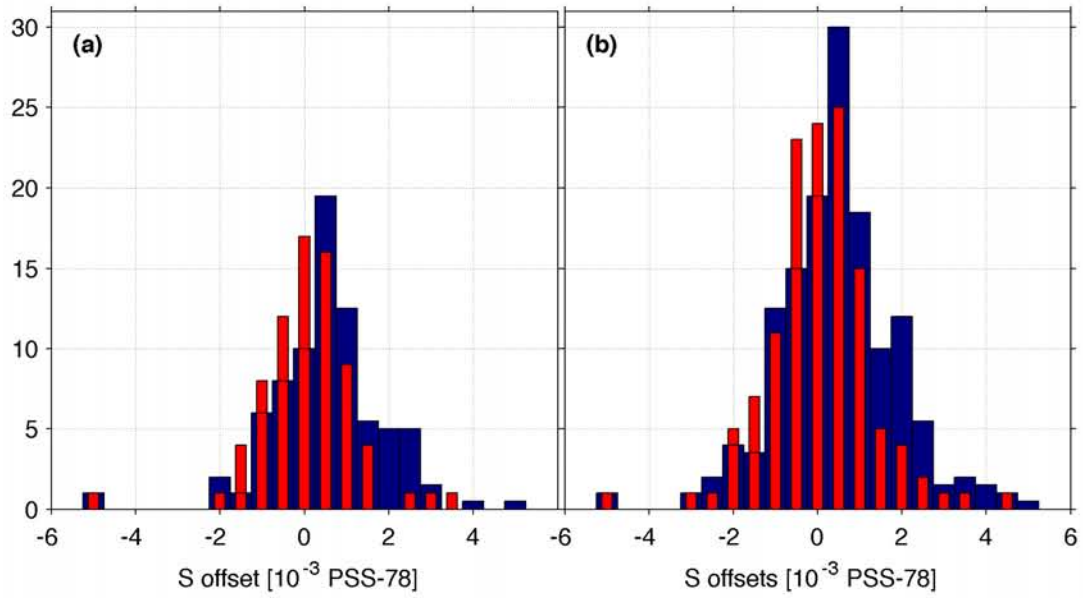


Figure A1: Histogram of estimated ad-hoc salinity offsets (red) and the sum of recommended SSW batch and ad-hoc salinity offsets (blue) applied to the CTD data along hydrographic legs in the (a) Southern Ocean and (b) Global Ocean (Table A1). If a leg had more than one SSW batch offset, each offset is given an equal weight in computing a mean.